Kishal Bipin Tandel
23MS115
October 14, 2025

Report 3

Instructors:
Prof. Satyabrata Raj
Prof. Goutam D. Mukherjee

PH3105: Nuclear Physics Laboratory

Abstract

In this experiment, the gamma-ray energy spectra of ^{60}Co and ^{137}Cs sources were analyzed using a NaI(Tl) scintillation detector coupled to a photomultiplier tube (PMT) and a Multi-Channel Analyzer (MCA). Calibration of the MCA was performed using the two characteristic γ-ray peaks of ^{60}Co at 1.17 MeV and 1.33 MeV. This calibration was then used to determine the photopeak energy of ^{137}Cs. The photopeak efficiency and the dependence of detector resolution on PMT voltage were also studied.

Contents

1 Introduction

Gamma-ray spectroscopy provides a quantitative method for measuring the energy and intensity of γ radiation emitted by radioactive sources. Each radionuclide emits photons with discrete energies, which serve as characteristic fingerprints for their identification. In this experiment, the γ spectra of ^{60}Co and ^{137}Cs were recorded using a NaI(Tl) scintillation detector, a photomultiplier tube (PMT), and a Multi-Channel Analyzer (MCA).

1.1 Aim

The aims of the experiment are as follows:

1. To calibrate the Multi-Channel Analyzer (MCA) using the two γ-ray photopeaks of ^{60}Co at 1.17 MeV and 1.33 MeV.
2. To determine the energy of the ^{137}Cs photopeak using the obtained calibration.
3. To compute the photopeak efficiency of ^{60}Co and ^{137}Cs peaks.
4. To study the variation of detector energy resolution as a function of PMT voltage.
5. To understand and interpret the characteristic features of γ-ray spectra such as photopeak, Compton continuum, Compton edge, and background.

1.2 Apparatus and Materials

The sources of γ ray photons in this experiment were radioactive ^{60}Co and ^{137}Cs. The detector was NaI(Tl) scintillation crystal which was optically coupled to a PMT and MCA. Data was acquired using *Spectrum Acquisition & Analysis Software*.

1.3 Experimental Setup and ^{137}Cs Source

The experimental set up is shown in Figure 1. The radioactive sources are shown in Figure 2.

Figure 1: Experimental setup

Figure 2: ^{60}Co (left) and ^{137}Cs (right)

2 Theory

2.1 Photon interactions with matter

Photons are quanta of electromagnetic radiation characterized by zero rest mass, no electric charge, and constant velocity c, the speed of light. Unlike charged particles, which continuously lose energy

through Coulombic interactions with matter, photons travel considerable distances without significant energy loss. Instead, they interact with matter through distinct mechanisms that result in partial or complete energy transfer to electrons. These secondary electrons subsequently deposit energy locally within the medium. Owing to this nature, photons are significantly more penetrating than charged particles of comparable energy.
The primary mechanisms by which photons interact with matter are the **photoelectric effect**, **Compton scattering**, and **pair production**. The probability of these interactions is quantified by the *linear attenuation coefficient* μ, which gives the probability of interaction per unit path length. It is material- and energy-dependent and is commonly expressed in units of cm^{-1}. By normalizing with respect to density ρ, one obtains the *mass attenuation coefficient* μ/ρ, expressed in cm^2/g.

2.1.1 Photoelectric effect

The photoelectric interaction results in the complete absorption of the incident photon and the ejection of a bound atomic electron. In the photoelectric process, a photon is completely absorbed by an atom, resulting in the ejection of an electron from an inner shell, typically the K-shell if the incident photon energy is sufficiently high. The kinetic energy of the emitted photoelectron is given by

$$E_{e^-} = h\nu - E_b$$

where $h\nu$ is the photon energy and E_b is the binding energy of the electron. The resulting vacancy in the atomic shell may lead to the emission of characteristic fluorescence X-rays. The photoelectric effect dominates at relatively low photon energies and for materials with high atomic number Z. Its probability τ is approximately proportional to

$$\tau \propto \frac{Z^n}{(h\nu)^3}, \quad \text{with } n \in [3, 4]$$

This strong Z-dependence explains why high-Z materials, such as lead, are effective shielding agents for low-energy photons. Photoelectric absorption is responsible for the full-energy (photo)peak in a detector when the entire photon energy is deposited. A schematic of Photoelectric Effect is shown in Figure 3.

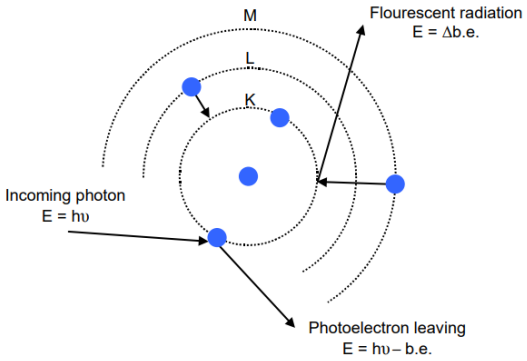

Figure 3: Schematic of Photoelectric Effect

2.1.2 Compton scattering

Compton scattering involves an inelastic collision between a photon and an essentially free or loosely bound electron. The photon is scattered at an angle θ relative to its incident direction, and a recoil electron (Compton electron) is ejected. The scattered photon has reduced energy,

$$h\nu' = \frac{h\nu}{1 + \frac{h\nu}{m_e c^2}(1 - \cos\theta)}$$

The corresponding energy imparted to the recoil electron is

$$E_{e^-} = h\nu - h\nu' = h\nu \left[1 - \frac{1}{1 + \frac{h\nu}{m_e c^2}(1 - \cos\theta)}\right]$$

The maximum kinetic energy transferred to the electron (Compton edge) occurs for backscatter $\theta = \pi$ and is given by

$$E_{e^-,\max} = h\nu \left(1 - \frac{1}{1 + \frac{2h\nu}{m_e c^2}}\right)$$

Compton scattering produces the continuous distribution below the photopeak with a sharp cutoff at the Compton edge. The Compton process is dominant in the intermediate energy range (100 keV–10 MeV) and is particularly significant for photon interactions in soft tissues. Its probability, denoted by σ, is nearly independent of Z, depending primarily on electron density. A schematic of Compton Scattering is shown in Figure 4.

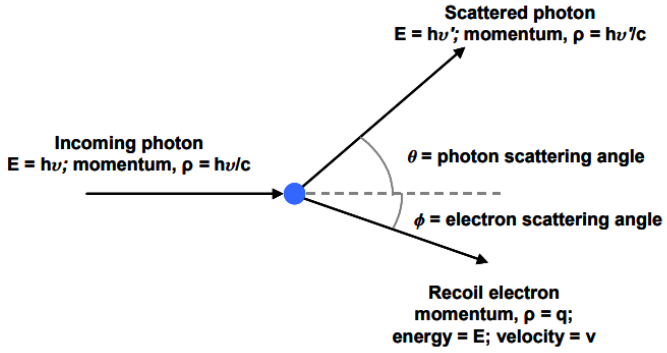

Figure 4: Schematic of Compton Scattering

2.1.3 Pair Production

When photon energy exceeds 1.022 MeV, interaction with the Coulomb field of a nucleus can lead to pair production. In this process, the photon disappears and is converted into an electron–positron pair:

$$h\nu \to e^- + e^+$$

The threshold energy corresponds to twice the electron rest energy ($2m_e c^2 = 1.022$ MeV). The kinetic energy of the created particles is

$$E_{e^-} + E_{e^+} = h\nu - 1.022\,\text{MeV}$$

The probability of pair production κ increases with photon energy and is approximately proportional to Z^2. The positron will eventually annihilate with an electron, producing two photons of 0.511 MeV each; if one or both of these annihilation photons escape the detector volume, escape peaks at $h\nu - 511$ keV (single-escape) and $h\nu - 1022$ keV (double-escape) appear in the spectrum. A schematic of Pair Production is shown in Figure 5.

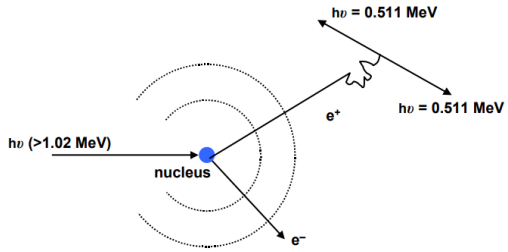

Figure 5: Schematic of Pair Production

2.1.4 Bulk Attenuation and Energy Deposition

The total attenuation coefficient is the sum of the contributions from all three processes:

$$\mu = \tau + \sigma + \kappa$$

Not all photon energy transferred to matter is absorbed locally. Some may escape as fluorescence photons or bremsstrahlung radiation. To describe the effective dose, one defines the energy-transfer coefficient μ_{tr} and the energy-absorption coefficient μ_{en}, where

$$\mu_{en} = \mu_{tr}(1 - g)$$

with g representing the fraction of transferred energy that escapes as radiative losses. The parameter μ_{en}/ρ is especially important in medical physics and radiation protection, as it directly relates to the absorbed dose.

In conclusion, photon interactions in matter are governed by three principal mechanisms, each dominating different energy regimes and showing distinct dependencies on photon energy and atomic number. These processes collectively determine photon penetration, shielding effectiveness, and energy deposition, which are crucial in fields such as diagnostic radiology, nuclear medicine, radiation therapy, and radiation shielding design. The plot showing the dominance of each of these three principal mechanisms in different energy regimes and for different atomic numbers is shown in Figure 6.

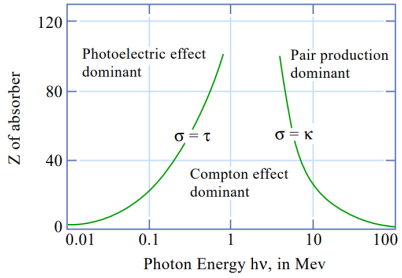

Figure 6: Atomic Number Z vs. Energy $h\nu$ (MeV)

2.2 Decay Scheme of ^{60}Co

Cobalt-60 (^{60}Co) is an artificial radionuclide produced by neutron activation of stable ^{59}Co in a nuclear reactor:

$$^{59}_{27}\mathrm{Co} + n \;\rightarrow\; ^{60}_{27}\mathrm{Co}$$

It is a strong γ-ray emitter with a half-life of

$$T_{1/2} = 5.27 \text{ years.}$$

The decay of ^{60}Co proceeds via β^- emission to excited states of nickel-60 (^{60}Ni*), followed by a cascade of two characteristic γ-ray transitions to the ground state. This makes ^{60}Co a widely used calibration and irradiation source.

2.2.1 Beta Decay

The decay process involves a β^- transition in which a neutron inside the cobalt nucleus converts into a proton, accompanied by the emission of an electron and an antineutrino:

$$n \;\rightarrow\; p + e^- + \bar{\nu}_e$$

At the nuclear level, this process transforms ^{60}Co (Z=27) into an excited ^{60}Ni (Z=28) nucleus:

$$^{60}_{27}\mathrm{Co} \;\rightarrow\; ^{60}_{28}\mathrm{Ni}^* + e^- + \bar{\nu}_e$$

Approximately 99.88% of the decays populate the excited ^{60}Ni nucleus at 2.505 MeV excitation energy, while a negligible branch (0.12%) goes directly to the ground state. The maximum (endpoint) energy of the emitted β^- spectrum is about 318 keV.

2.2.2 Gamma-Ray Cascade

The excited ^{60}Ni* nucleus de-excites to the ground state through a two-step γ-ray cascade:

$$^{60}_{28}\mathrm{Ni}^*(2505 \text{ keV}) \xrightarrow[\gamma_1]{E_{\gamma_1}=1.173 \text{ MeV}} {}^{60}_{28}\mathrm{Ni}^*(1332 \text{ keV}) \xrightarrow[\gamma_2]{E_{\gamma_2}=1.332 \text{ MeV}} {}^{60}_{28}\mathrm{Ni}_{(\text{ground})}$$

Thus, each ^{60}Co decay event typically results in the emission of two nearly simultaneous γ-ray photons with energies of 1.17 MeV and 1.33 MeV, in addition to the β^- particle and antineutrino. Because these γ rays are emitted in cascade and are well separated in energy, they produce two distinct peaks in a γ-ray energy spectrum obtained using a scintillation or semiconductor detector.

2.2.3 Internal Conversion and Coincidence Effects

As in most nuclear de-excitations, a small fraction of the transitions in ^{60}Ni* can proceed via internal conversion, in which the transition energy is transferred directly to an orbital electron, which is then ejected. However, for ^{60}Co, the internal conversion coefficients are very small ($\alpha \lesssim 0.002$), so γ emission dominates overwhelmingly.

Because the two γ rays are emitted in rapid succession (within picoseconds), coincidence summing can occur if both photons are detected simultaneously, producing a small sum peak around 2.505 MeV in high-efficiency detectors.

2.2.4 Summary of Decay Scheme

The decay scheme of ^{60}Co can be summarized as follows:

$$\begin{aligned} {}^{60}_{27}\mathrm{Co} &\xrightarrow[\beta^-,\,99.88\%]{T_{1/2}=5.27\ \mathrm{y}} {}^{60}_{28}\mathrm{Ni}^*(2505\ \mathrm{keV}) + e^- + \bar{\nu}_e \\ {}^{60}_{28}\mathrm{Ni}^*(2505\ \mathrm{keV}) &\xrightarrow[\gamma_1]{} {}^{60}_{28}\mathrm{Ni}^*(1332\ \mathrm{keV}) + \gamma(1.173\ \mathrm{MeV}) \\ {}^{60}_{28}\mathrm{Ni}^*(1332\ \mathrm{keV}) &\xrightarrow[\gamma_2]{} {}^{60}_{28}\mathrm{Ni}_{(\mathrm{g.s.})} + \gamma(1.332\ \mathrm{MeV}) \end{aligned}$$

Therefore, ^{60}Co serves as an excellent dual-line γ-ray calibration source, emitting photons at 1.17 MeV and 1.33 MeV with nearly equal intensities (each ≈99.9%), making it invaluable for efficiency and energy calibration in γ-ray spectroscopy.

2.3 Decay Scheme of ^{137}Cs

Cesium-137 (^{137}Cs) is a radioactive fission product with a half-life of

$$T_{1/2} = 30.17 \text{ years}$$

It decays predominantly by β^- emission to an excited state of barium-137 ($^{137\mathrm{m}}$Ba), which then de-excites by emitting a characteristic gamma ray. The overall decay scheme is therefore a two-step process: a nuclear β^- decay followed by an electromagnetic de-excitation.

2.3.1 Beta Decay

The primary decay mode of ^{137}Cs is β^- decay, in which a neutron in the nucleus transforms into a proton, accompanied by the emission of an electron (the beta particle) and an antineutrino:

$$n \;\rightarrow\; p + e^- + \bar{\nu}_e$$

At the nuclear level, this transforms ^{137}Cs (Z=55) into an excited state of ^{137}Ba (Z=56). The reaction can be written as

$${}^{137}_{55}\mathrm{Cs} \;\rightarrow\; {}^{137\mathrm{m}}_{56}\mathrm{Ba}^* + e^- + \bar{\nu}_e$$

About 94.6% of the decays populate the metastable isomeric state $^{137\mathrm{m}}$Ba at 661.7 keV excitation energy. A much smaller fraction ($\sim$ 5.4%) directly populates the ground state of ^{137}Ba. The endpoint energy of the emitted beta spectrum in the main branch is approximately 1.176 MeV, while in the minor branch it is about 514 keV.

2.3.2 Isomeric Transition and Gamma Emission

The metastable $^{137\mathrm{m}}$Ba state has a half-life of

$$T_{1/2} = 2.55 \text{ minutes}$$

It de-excites almost exclusively via electromagnetic processes. The most probable mode is gamma emission, in which a 661.7 keV photon is emitted:

$${}^{137\mathrm{m}}_{56}\mathrm{Ba} \;\rightarrow\; {}^{137}_{56}\mathrm{Ba}_{(\mathrm{ground})} + \gamma\,(661.7\ \mathrm{keV})$$

This 662 keV gamma ray is the prominent line observed in scintillation spectroscopy of ^{137}Cs and is the basis for its widespread use as a calibration source in gamma-ray detectors.

2.3.3 Internal Conversion

In addition to gamma-ray emission, the excited $^{137\mathrm{m}}$Ba nucleus can also decay via the process of internal conversion. In this process, instead of emitting a gamma ray, the nucleus transfers its excitation energy directly to one of its own orbital electrons, which is then ejected from the atom:

$$^{137\mathrm{m}}_{56}\mathrm{Ba} \;\rightarrow\; ^{137}_{56}\mathrm{Ba}_{(\mathrm{ground})} + e^-_{\mathrm{IC}}$$

The probability of internal conversion relative to gamma emission is described by the *internal conversion coefficient* (ICC), defined as

$$\alpha = \frac{N_{\mathrm{IC}}}{N_\gamma}$$

where N_{IC} is the number of internal conversion electrons and N_γ is the number of gamma photons emitted. For $^{137\mathrm{m}}$Ba, the ICC for the 661.7 keV transition is approximately $\alpha \approx 0.12$. Thus, about 12% as many conversion electrons are emitted as gamma rays. The ejection of inner-shell electrons also leads to the emission of characteristic X-rays from barium as the atomic vacancies are filled.

2.3.4 Summary of Decay Scheme

The complete decay scheme of ^{137}Cs can be summarized as follows:

$$\begin{aligned}
^{137}_{55}\mathrm{Cs} &\xrightarrow[\beta^-,\,94.6\%]{T_{1/2}=30.17\,\mathrm{y}} {}^{137\mathrm{m}}_{56}\mathrm{Ba}\,(661.7\ \mathrm{keV}) + e^- + \bar{\nu}_e \\
^{137\mathrm{m}}_{56}\mathrm{Ba} &\xrightarrow[\gamma,\,85.1\%]{T_{1/2}=2.55\,\mathrm{min}} {}^{137}_{56}\mathrm{Ba}_{(\mathrm{g.s.})} + \gamma\,(661.7\ \mathrm{keV}) \\
^{137\mathrm{m}}_{56}\mathrm{Ba} &\xrightarrow[\mathrm{IC},\,11\%]{} {}^{137}_{56}\mathrm{Ba}_{(\mathrm{g.s.})} + e^-_{\mathrm{IC}} \\
^{137}_{55}\mathrm{Cs} &\xrightarrow[\beta^-,\,5.4\%]{} {}^{137}_{56}\mathrm{Ba}_{(\mathrm{g.s.})} + e^- + \bar{\nu}_e
\end{aligned}$$

Thus, the ^{137}Cs decay chain provides a nearly monoenergetic 662 keV gamma ray with high intensity, making it an ideal source for energy calibration in gamma spectroscopy.

2.4 NaI(Tl) Scintillation Detector

The fundamental principle of a scintillation detector is the conversion of ionizing radiation into visible light photons, which can then be detected by a photosensitive device. In this experiment, a thallium-doped sodium iodide [NaI(Tl)] scintillation crystal is used. Sodium iodide is an inorganic scintillator with a high atomic number ($Z = 53$ for iodine), giving it a large photoelectric cross-section and therefore high detection efficiency for medium-energy gamma rays such as the 662 keV photon from ^{137}Cs. The addition of thallium, in concentrations of approximately 0.1% by weight, introduces activator sites in the crystal lattice that are essential for efficient scintillation.

When a gamma ray enters the NaI(Tl) crystal, it interacts with the material via one of the standard gamma-ray interaction mechanisms: the photoelectric effect, Compton scattering, or pair production (though the latter is absent at 662 keV). In each case, energetic secondary electrons are produced. These electrons lose their energy primarily through ionization and excitation of the crystal lattice. The excitation energy is then transferred to the thallium activator sites. The excited thallium ions subsequently return to their ground state by emitting photons in the visible region, typically centered around 410 nm. This emission is well matched to the spectral sensitivity of photomultiplier tubes.

The NaI(Tl) scintillator has several important characteristics that make it suitable for gamma spectroscopy. Firstly, it exhibits a high light yield, approximately 38,000 photons per MeV of absorbed gamma-ray energy, which translates to good energy resolution. Secondly, its scintillation decay time is relatively short (around 230 ns), allowing for the detection of events at high counting rates. Thirdly, NaI(Tl) crystals can be manufactured in large sizes, increasing detection efficiency for weak or extended sources. However, the material is hygroscopic and readily absorbs moisture from the atmosphere, so the crystal must be hermetically sealed in an aluminum housing with a transparent optical window for coupling to the photomultiplier tube. In the present experiment, the NaI(Tl) scintillator is responsible for converting the discrete gamma-ray energies of ^{137}Cs into flashes of light proportional to the deposited energy.

2.5 Photomultiplier Tube (PMT)

The scintillation light emitted by the NaI(Tl) crystal is too faint to be measured directly using ordinary electronics. Therefore, it is coupled optically to a photomultiplier tube (PMT), which acts as an extremely sensitive light detector with high gain. A PMT consists of three main functional components: a photocathode, a series of dynodes, and an anode.

The photocathode is a thin photosensitive layer deposited on the inner surface of the PMT window. When photons from the scintillator strike the photocathode, they liberate electrons via the photoelectric effect. The probability of photon-to-electron conversion is described by the quantum efficiency of the photocathode, which is typically in the range of 20–30% at 410 nm for commonly used bialkali photocathodes. The emitted electrons are referred to as photoelectrons, and the number of photoelectrons generated is directly proportional to the intensity of the scintillation light, and hence to the energy deposited in the scintillator by the gamma ray.

The photoelectrons are then accelerated and focused onto the first dynode by an applied high voltage (usually several hundred to over one thousand volts across the tube). When a photoelectron strikes the dynode, secondary emission occurs: several electrons are ejected for each incident electron. This multiplication process is repeated at each successive dynode stage, with typical PMTs containing 8 to 14 dynodes. The overall electron multiplication, or gain, can be as high as 10^6 to 10^7, amplifying the signal from just a handful of photoelectrons to a measurable current pulse. The final electron cloud is collected at the anode, resulting in a sharp voltage pulse at the PMT output. The amplitude of this pulse is proportional to the original energy deposition in the scintillator, allowing pulse-height spectroscopy to be performed.

The PMT is therefore an indispensable part of the scintillation detection system. It combines high sensitivity to single photons, large internal gain, and nanosecond time resolution. However, it is also sensitive to noise such as thermionic emission from the photocathode (dark current) and afterpulsing. Proper biasing of the PMT and shielding from ambient light are essential for stable operation. In this experiment, the PMT provides the electrical pulses that carry the gamma-ray energy information after detection in the scintillator.

2.6 Multi-Channel Analyzer (MCA)

The electrical pulses produced at the output of the photomultiplier tube vary in amplitude according to the energy deposited in the NaI(Tl) scintillator by the incident gamma rays. To obtain the energy spectrum efficiently, these pulses are analyzed by a Multi-Channel Analyzer (MCA) rather than a Single Channel Analyzer.

An MCA is an electronic system that measures the amplitude of each incoming pulse, converts it into a digital number proportional to the pulse height, and sorts it into one of many channels corresponding to discrete energy bins. The total number of channels typically ranges from 256 up to 8192 or more, depending on the resolution and memory capacity of the device. In this way, the MCA simultaneously records the full distribution of pulse heights, producing a histogram of *counts versus channel number* that directly represents the gamma-ray energy spectrum.

Internally, an MCA consists of three principal stages: a pulse amplifier, an analog-to-digital converter (ADC), and a memory or multichannel storage unit. The amplifier shapes and standardizes the PMT pulses. The ADC then samples each pulse and assigns it to a digital value proportional to its height. This value designates the channel number in which the count is accumulated. The resulting spectrum can be displayed on a computer interface, showing characteristic photopeaks, Compton continua, and other spectral features.

Compared to an SCA, which requires manual scanning of the discriminator window to reconstruct the spectrum point by point, the MCA provides a significant improvement in speed, resolution, and statistical accuracy. It captures the entire spectrum in a single acquisition period, enabling detailed quantitative analysis such as energy calibration, peak area determination, and computation of the detector's energy resolution.

In the present experiment, the MCA was used in conjunction with the NaI(Tl) scintillation detector and PMT to record the gamma-ray spectra of ^{137}Cs and ^{60}Co. The resulting spectra display distinct photopeaks at 662 keV for ^{137}Cs and at 1.17 MeV and 1.33 MeV for ^{60}Co, along with their corresponding Compton continua. These peaks serve as the experimental basis for gamma-ray spectroscopy and detector calibration.

2.7 Efficiency of the Scintillation Detector

In gamma-ray spectroscopy, an important characteristic of the detector is its **efficiency**, which quantifies the fraction of detected events that contribute to the full-energy photopeak relative to the total number of detected events. In this experiment, the efficiency is evaluated in terms of the **photopeak efficiency** ε_{p}, defined as the ratio of the counts under the photopeak to the total counts in the spectrum:

$$\varepsilon_{\mathrm{p}} = \frac{\text{Area under the photopeak}}{\text{Total area under the spectrum}} \tag{2.7.1}$$

The photopeak area represents gamma rays that have deposited their full energy in the detector, typically via the photoelectric effect, while the total area of the spectrum includes all events, such as partial-energy depositions from Compton scattering and background counts. Thus, the photopeak efficiency provides a measure of the detector's ability to accurately register full-energy events relative to all interactions.

Factors affecting the photopeak efficiency include:

1) Detector size and geometry: Larger crystals subtend a greater solid angle relative to the source, increasing the probability of gamma-ray interaction.

2) Gamma-ray energy: Higher-energy photons have a lower probability of complete absorption, reducing the photopeak efficiency.

3) Source-detector distance: Increasing distance reduces the fraction of emitted photons incident on the detector.

4) Detector material: The high atomic number of NaI(Tl) improves the likelihood of photoelectric absorption, enhancing the photopeak contribution.

In the present experiment, the photopeak efficiency is determined by integrating the counts under the photopeak of ^{137}Cs (662 keV) and ^{60}Co (1.17 MeV and 1.33 MeV) and dividing by the total counts in the recorded spectrum. This provides a simple yet quantitative measure of the detector's ability to accurately register full-energy gamma interactions and is crucial for calibration and quantitative gamma-ray spectroscopy.

2.8 Energy Resolution of the Scintillation Detector

One of the key performance characteristics of a scintillation spectrometer is its **energy resolution**, which quantifies the detector's ability to distinguish between two gamma rays of closely spaced energies. In practice, when a monoenergetic gamma ray such as the 661.7 keV photon from ^{137}Cs interacts with the NaI(Tl) detector, the resulting photopeak in the pulse height spectrum is not a sharp line but rather has a finite width. This broadening arises primarily from statistical fluctuations in the number of scintillation photons produced, the number of photoelectrons emitted at the PMT photocathode, and subsequent variations in the electron multiplication process. Additional contributions come from non-uniform light collection within the crystal, electronic noise in the signal chain, and intrinsic properties of the scintillator such as non-proportionality of light yield.

The photopeak in the measured spectrum is generally well described by a Gaussian distribution, with its width characterized by the full width at half maximum (FWHM). The **energy resolution** R of the detector at a gamma-ray energy E is therefore defined as

$$R(E) \;=\; \frac{\Delta E}{E} \tag{2.8.1}$$

where ΔE is the FWHM of the photopeak (expressed in the same energy units as E). This definition provides a dimensionless measure of the sharpness of the peak.

From a theoretical standpoint, the energy resolution is ultimately limited by the statistics of photon generation and detection. If N represents the average number of photoelectrons produced per absorbed gamma ray, then the statistical fluctuation in this number follows Poisson statistics, with standard deviation $\sqrt{N}$. The corresponding relative uncertainty scales as $1/\sqrt{N}$. Since N is proportional to the deposited energy E, the statistical contribution to the resolution is expected to scale as

$$R(E) \;\propto\; \frac{1}{\sqrt{E}}$$

This dependence explains why scintillation detectors have better (i.e., smaller) resolution at higher gamma-ray energies.

In practice, the measured energy resolution of NaI(Tl) detectors at 662 keV is typically in the range of 6–10%, depending on the crystal quality, size, optical coupling to the PMT, and electronic processing. While this resolution is inferior to that of semiconductor detectors such as high-purity germanium (HPGe), it is adequate for many applications, particularly when high efficiency and robustness are required.

3 MCA Caliberation

Using a ^{60}Co source, we performed data acquisition for 600 s at PMT high voltage 610 V. The resulting histogram is shown in Fig 7 and the fitted peaks are shown in Fig 8.

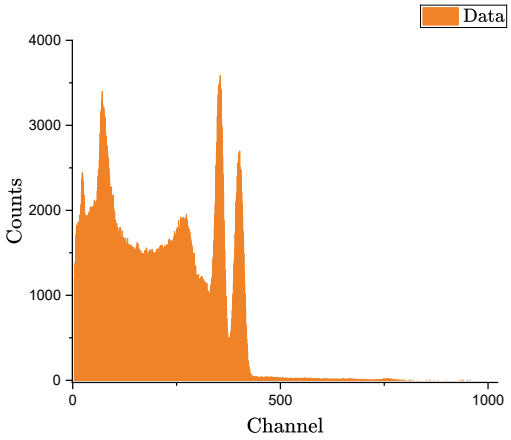

Figure 7: ^{60}Co Spectrum

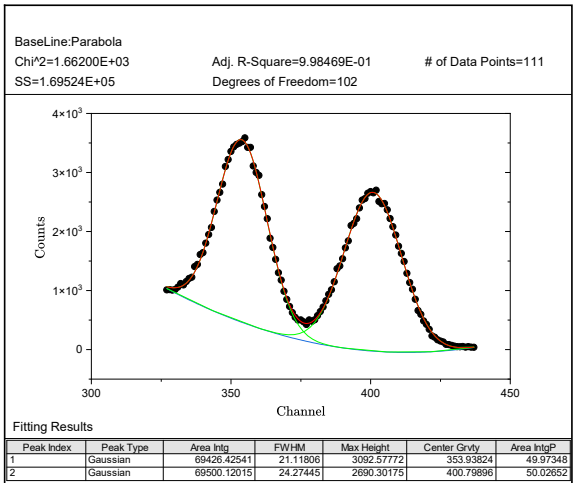

Peak Index	Peak Type	Area Intg	FWHM	Max Height	Center Grvty	Area IntgP
1	Gaussian	69426.42541	21.11806	3092.57772	353.93824	49.97348
2	Gaussian	69500.12015	24.27445	2690.30175	400.79896	50.02652

Figure 8: ^{60}Co Peaks fitted by sum of two Gaussians and a quadratic polynomial

Since Energy $E \propto$ Voltage Pulse $V \propto$ Channel Number C, we will use a linear caliberation model as follows:

$$E = aC + b \tag{3.1}$$

where a and b are constants to be determined. If we have two energies E_1 and E_2 corresponding to two channel numbers C_1 and C_2, using Eq.(3.1), the constants a and b are given by:

$$a = \frac{E_1 - E_2}{C_1 - C_2} \qquad \& \qquad b = \frac{E_1 C_2 - E_2 C_1}{C_2 - C_1} \tag{3.2}$$

Using known γ lines of ^{60}Co and using Fig 8, we get energy $E_1 = 1.17$ MeV corresponds to channel number $C_1 \approx 353.94$ and energy $E_2 = 1.33$ MeV corresponds to channel number $C_2 \approx 400.80$. Using these values in Eq.(3.2), we get:

$$a = 3.41 \times 10^{-3} \text{ Mev/Channel} \qquad \& \qquad b = -3.85 \times 10^{-2} \text{ Mev} \tag{3.3}$$

Using Eq. (3.3) in Eq. (3.1), the MCA caliberation equation is:

$$E = (3.41 \times 10^{-3})C - (3.85 \times 10^{-2}) \text{ MeV} \tag{3.4}$$

Using Eq. (3.4), we can write:

$$\Delta E = (3.41 \times 10^{-3})\Delta C \tag{3.5}$$

4 Determination of ^{137}Cs Peak Energy

Using a ^{137}Cs source, we performed data acquisition for 600 s at PMT high voltage 610 V. The resulting histogram is shown in Fig 9 and the fitted peak is shown in Fig 10.

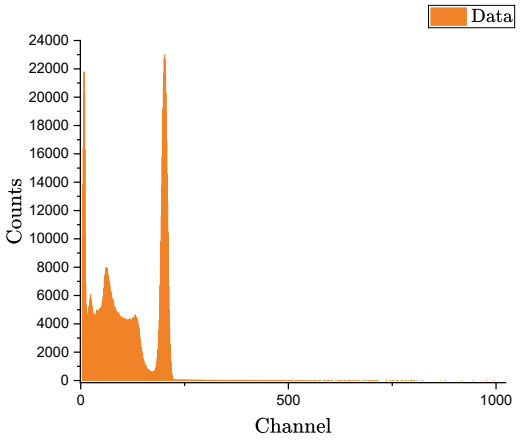

Figure 9: ^{137}Cs Spectrum

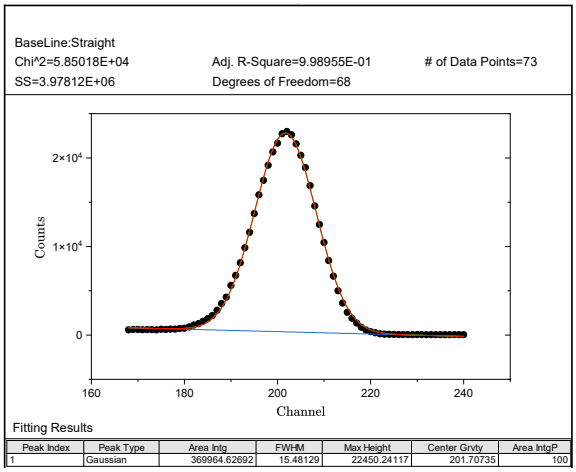

Figure 10: ^{137}Cs Peak fitted by the sum of a Gaussian and a straight line

Using Fig 10, we find that the photopeak corresponds to channel number $C \approx 201.71$. Substituting this value in Eq. (3.4), we find the energy of the photopeak to be $E \approx 0.65$ MeV. We will now calculate the error associated with this determined photopeak energy $E = 0.65$ MeV. The Literature value is $E = 0.66$ MeV.

1) Absolute Error = |Determined Value - Literature Value| = |0.65 - 0.66| = 0.01 MeV

2) Relative Error = Absolute Error/Literature Value = $0.01/0.66 \approx 0.015$

3) Percentage Error = Relative Error x 100% = 0.015 x 100% = 1.5%

5 Photopeak Efficiency

We already found the area under peaks of ^{60}Co and ^{137}Cs as given in Fig 8 and Fig 10 respectively. The area under spectrum of ^{60}Co and ^{137}Cs is calculated using *OriginPro Graphing & Analysis Software*. The photopeak efficiency is calculated as given by Eq. (2.7.1) and the results are listed in Table 1.

Source	Photopeak Energy (MeV)	Area under Peak	Area under Spectrum	Photopeak Efficiency
^{60}Co	1.17	69426.43	742055.00	0.0936
^{60}Co	1.33	69500.12	742055.00	0.0937
^{137}Cs	0.65	369964.63	1229797.00	0.3008

Table 1: Photopeak Efficiency

From Table 1, the photopeak efficiencies for ^{60}Co at 1.17 MeV and 1.33 MeV are 0.0936 and 0.0937, respectively, showing consistent detector response. The ^{137}Cs source at 0.65 MeV shows a higher efficiency of 0.3008. This indicates that photopeak efficiency decreases with increasing gamma energy, as higher-energy photons have a lower interaction probability within the detector.

6 Variation of Resolution with PMT Voltage

We varied PMT High Voltage and performed data acquisition for 300 s at each voltage using ^{60}Co. The spectrum obtained and the corresponding fitted peaks for each voltage are shown below:

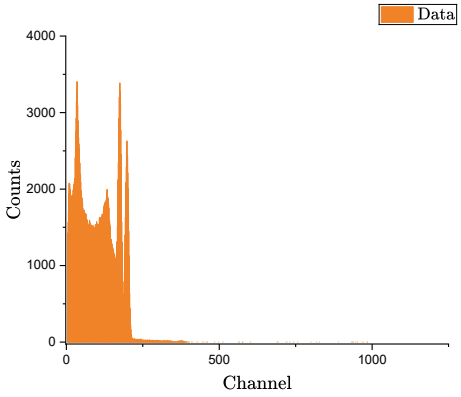

Figure 11: ^{60}Co Spectrum at 540 V

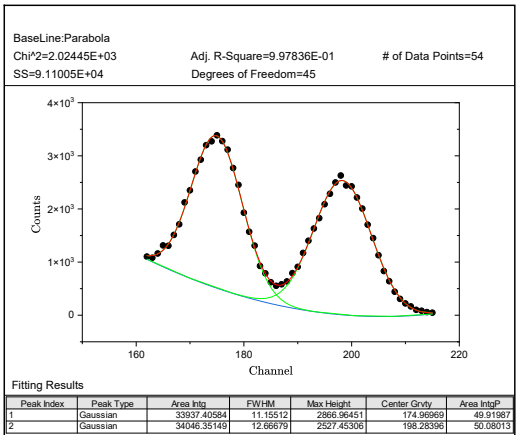

Figure 12: Fitted ^{60}Co Peaks at 540 V

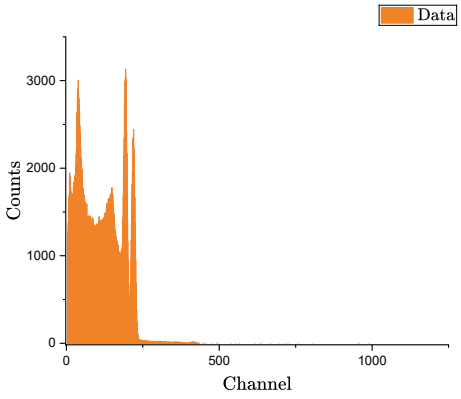

Figure 13: ^{60}Co Spectrum at 550 V

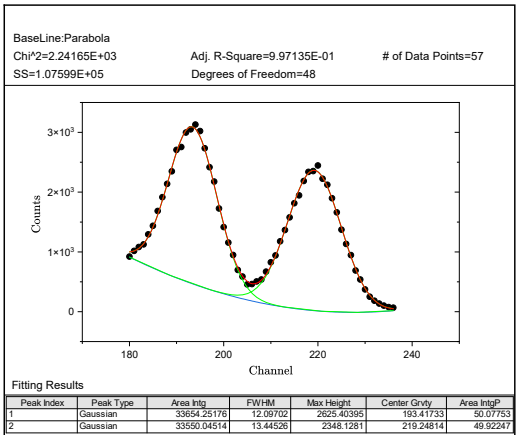

Figure 14: Fitted ^{60}Co Peaks at 550 V

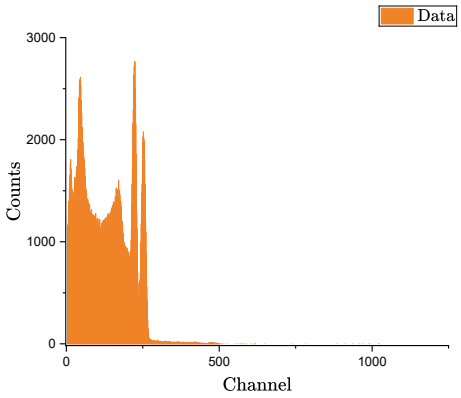

Figure 15: ^{60}Co Spectrum at 560 V

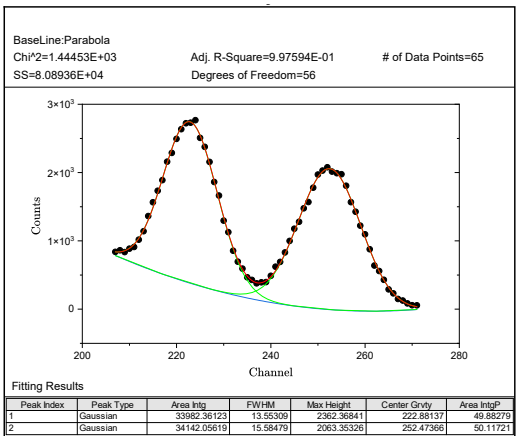

Figure 16: Fitted ^{60}Co Peaks at 560 V

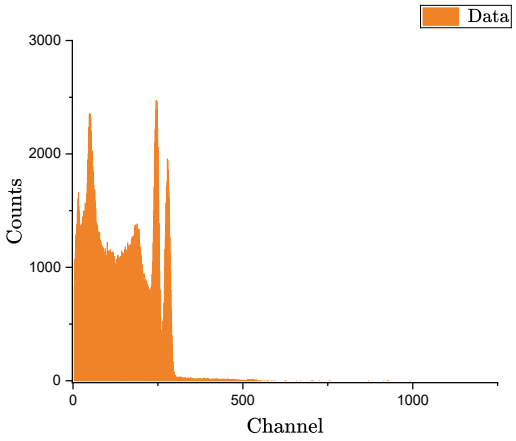

Figure 17: ^{60}Co Spectrum at 570 V

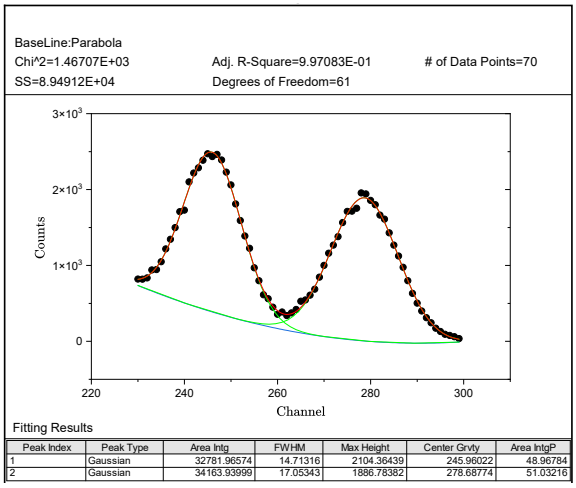

Peak Index	Peak Type	Area Intg	FWHM	Max Height	Center Grvty	Area IntgP
1	Gaussian	32781.96574	14.71316	2104.36439	245.96022	48.96784
2	Gaussian	34163.93999	17.05343	1886.78382	278.68774	51.03216

Figure 18: Fitted ^{60}Co Peaks at 570 V

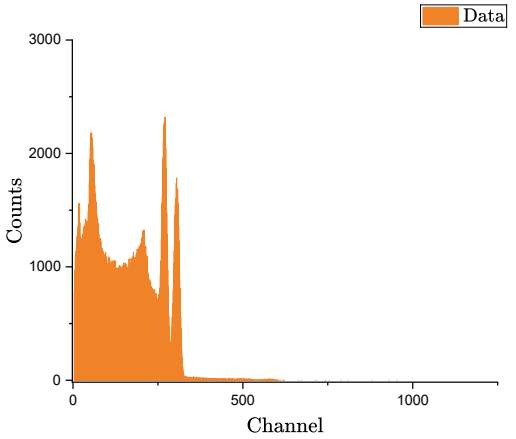

Figure 19: ^{60}Co Spectrum at 580 V

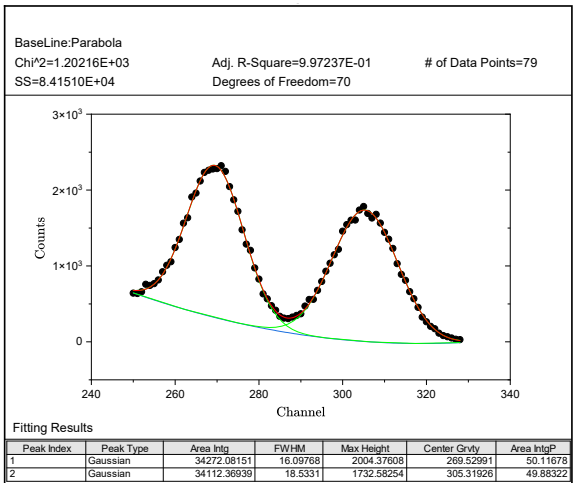

Peak Index	Peak Type	Area Intg	FWHM	Max Height	Center Grvty	Area IntgP
1	Gaussian	34272.08151	16.09768	2004.37608	269.52991	50.11678
2	Gaussian	34112.36939	18.5331	1732.58254	305.31926	49.88322

Figure 20: Fitted ^{60}Co Peaks at 580 V

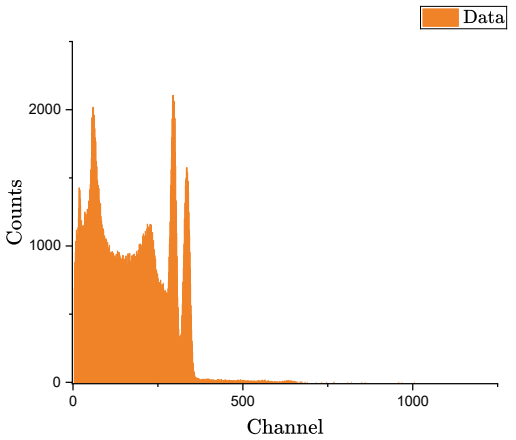

Figure 21: ^{60}Co Spectrum at 590 V

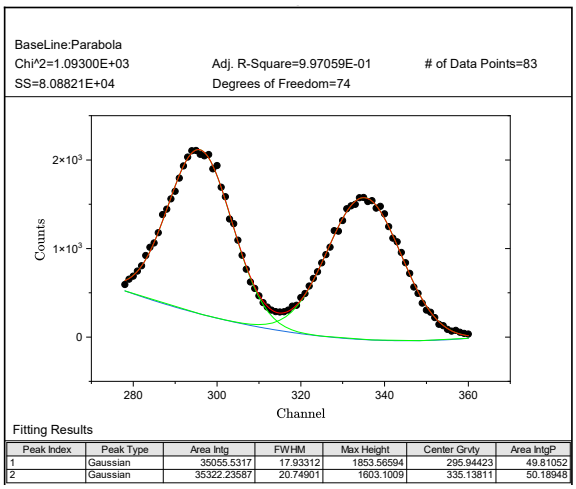

Peak Index	Peak Type	Area Intg	FWHM	Max Height	Center Grvty	Area IntgP
1	Gaussian	35055.5317	17.93312	1853.56594	295.94423	49.81052
2	Gaussian	35322.23587	20.74901	1603.1009	335.13811	50.18948

Figure 22: Fitted ^{60}Co Peaks at 590 V

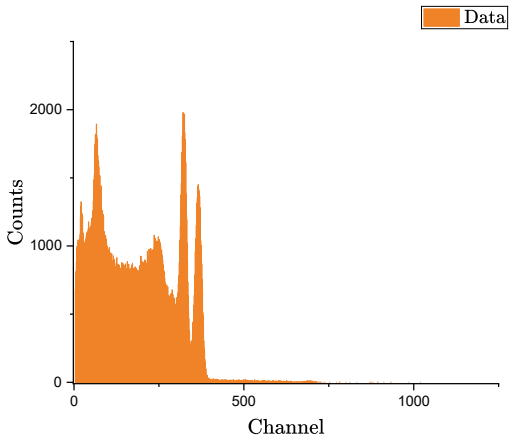

Figure 23: ^{60}Co Spectrum at 600 V

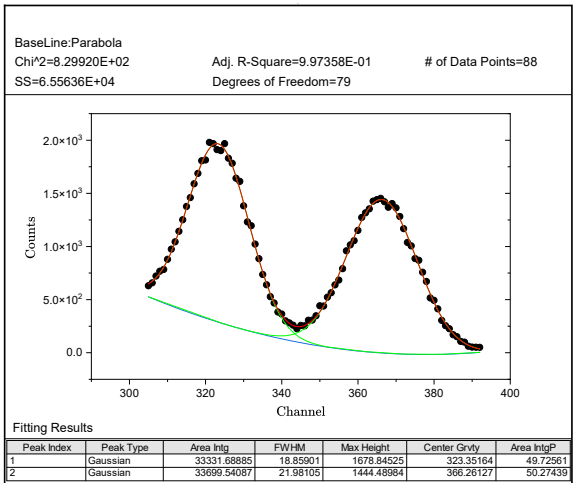

Figure 24: Fitted ^{60}Co Peaks at 600 V

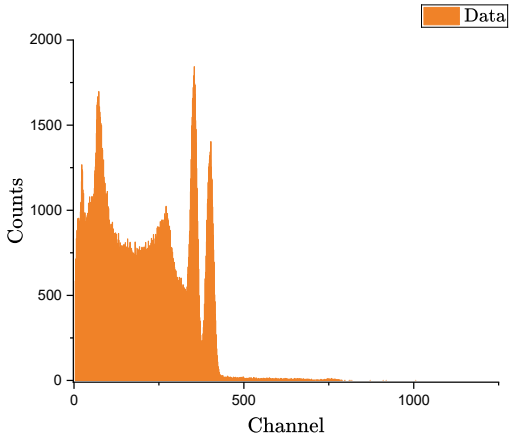

Figure 25: ^{60}Co Spectrum at 610 V

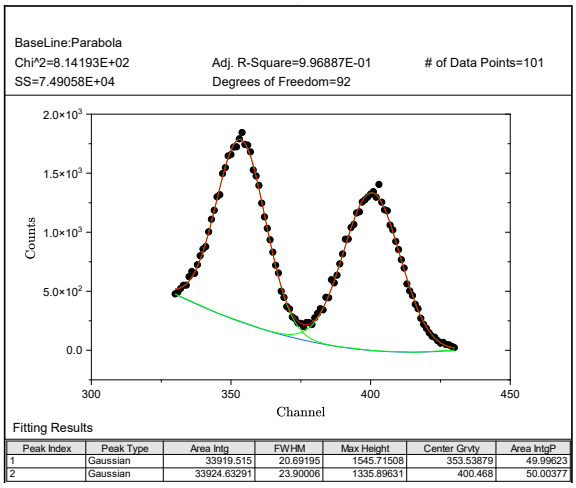

Figure 26: Fitted ^{60}Co Peaks at 610 V

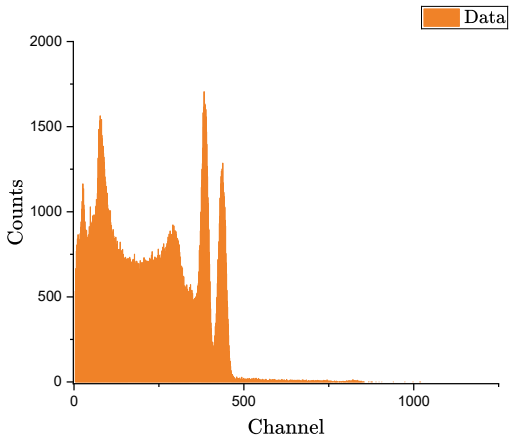

Figure 27: ^{60}Co Spectrum at 620 V

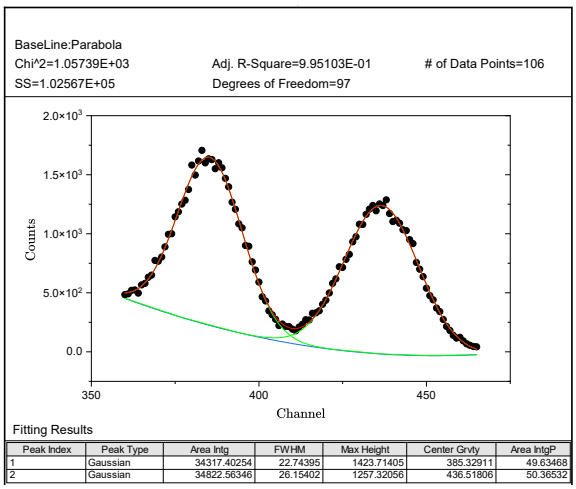

Figure 28: Fitted ^{60}Co Peaks at 620 V

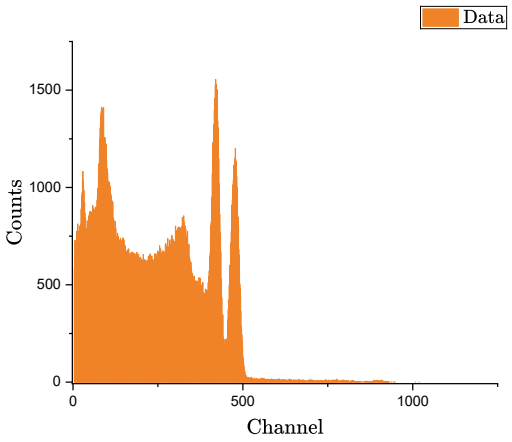

Figure 29: ^{60}Co Spectrum at 6300 V

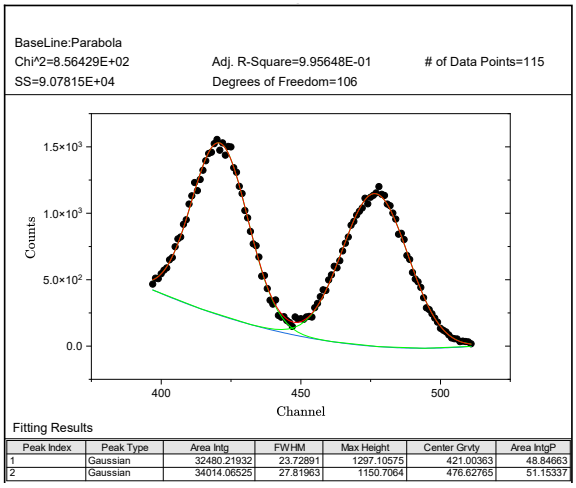

Peak Index	Peak Type	Area Intg	FWHM	Max Height	Center Grvty	Area IntgP
1	Gaussian	32480.21932	23.72891	1297.10575	421.00363	48.84663
2	Gaussian	34014.06525	27.81963	1150.7064	476.62765	51.15337

Figure 30: Fitted ^{60}Co Peaks at 630 V

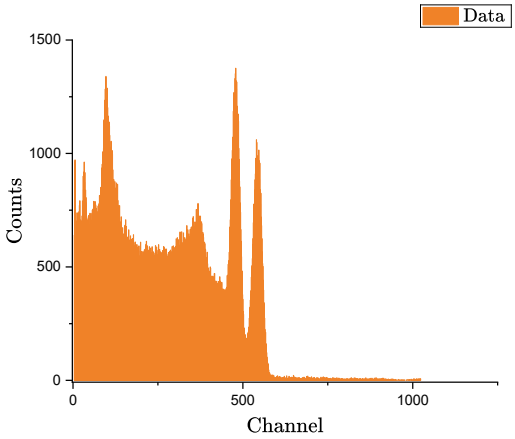

Figure 31: ^{60}Co Spectrum at 640 V

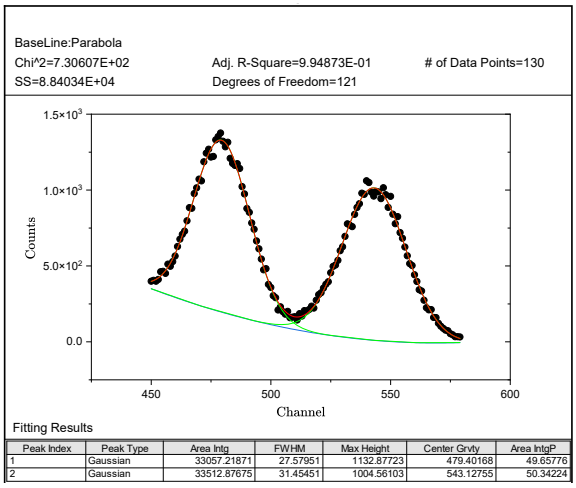

Peak Index	Peak Type	Area Intg	FWHM	Max Height	Center Grvty	Area IntgP
1	Gaussian	33057.21871	27.57951	1132.87723	479.40168	49.65776
2	Gaussian	33512.87675	31.45451	1004.56103	543.12755	50.34224

Figure 32: Fitted ^{60}Co Peaks at 640 V

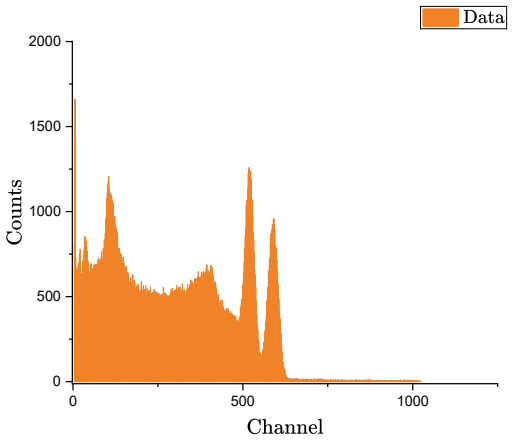

Figure 33: ^{60}Co Spectrum at 650 V

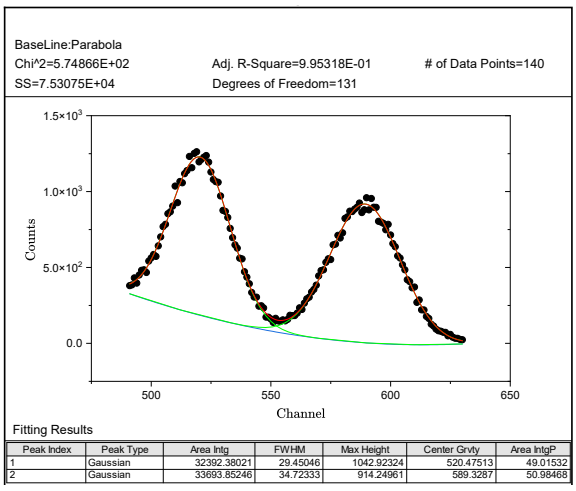

Peak Index	Peak Type	Area Intg	FWHM	Max Height	Center Grvty	Area IntgP
1	Gaussian	32392.38021	29.45046	1042.92324	520.47513	49.01532
2	Gaussian	33693.85246	34.72333	914.24961	589.3287	50.98468

Figure 34: Fitted ^{60}Co Peaks at 650 V

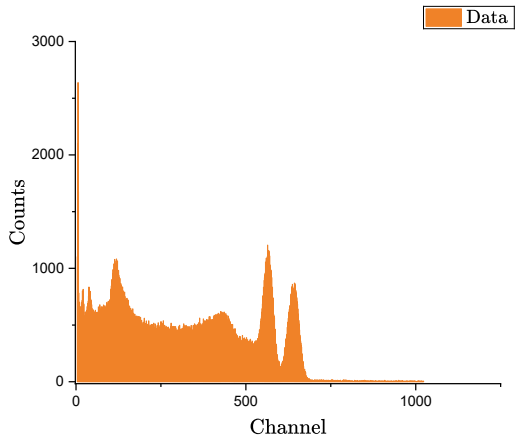

Figure 35: ^{60}Co Spectrum at 660 V

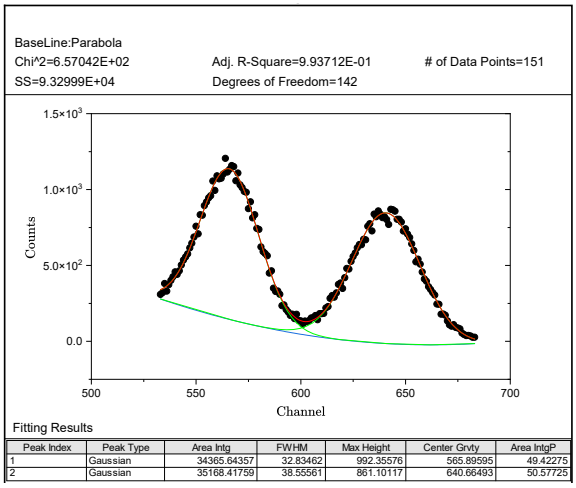

Figure 36: Fitted ^{60}Co Peaks at 660 V

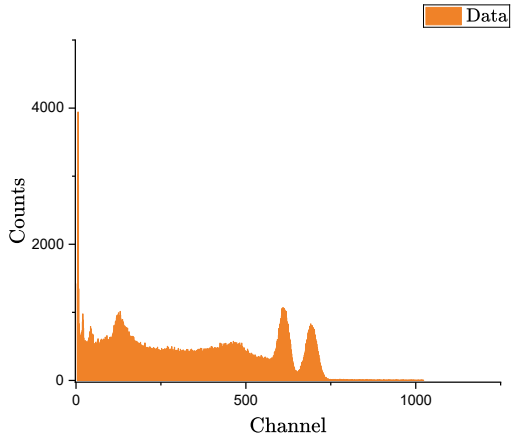

Figure 37: ^{60}Co Spectrum at 670 V

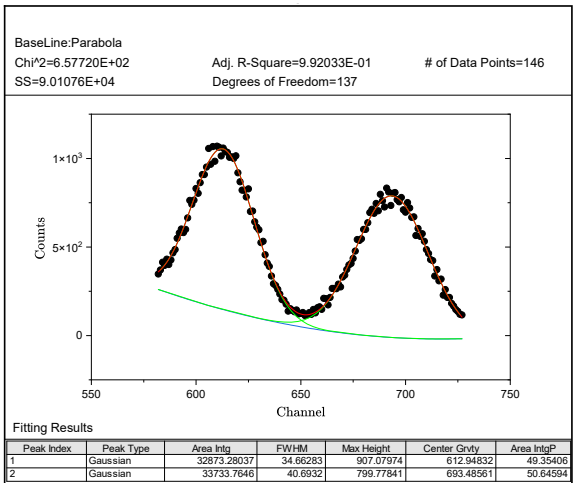

Figure 38: Fitted ^{60}Co Peaks at 670 V

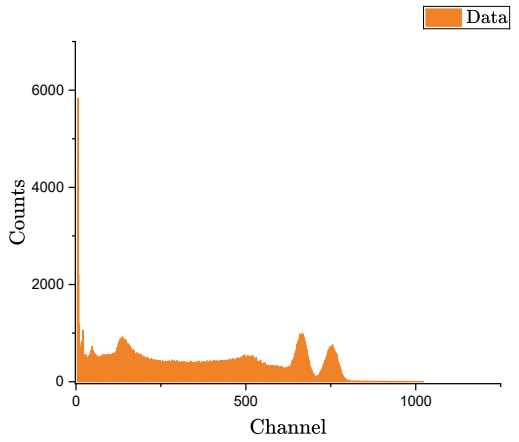

Figure 39: ^{60}Co Spectrum at 680 V

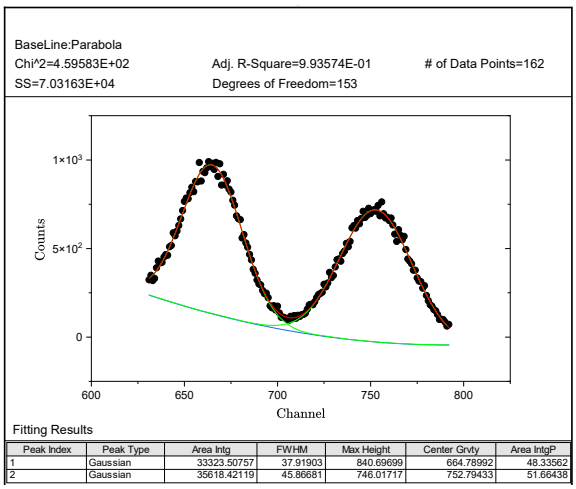

Figure 40: Fitted ^{60}Co Peaks at 680 V

Using these graphs and Eqs. (2.8.1), (3.4) and (3.5), we find the resolution at different PMT Voltages. $E_1, \Delta E_1, r_1$ and $E_2, \Delta E_2, r_2$ are for first and second ^{60}Co peaks respectively. We have listed these in the Table 2.

High Voltage (V)	E_1 (MeV)	ΔE_1 (MeV)	Resolution r_1	E_2 (MeV)	ΔE_2 (MeV)	Resolution r_2
540	0.5582	0.0380	0.0682	0.6377	0.0432	0.0677
550	0.6211	0.0413	0.0664	0.7091	0.0459	0.0647
560	0.7215	0.0462	0.0641	0.8224	0.0531	0.0646
570	0.8002	0.0502	0.0627	0.9118	0.0582	0.0638
580	0.8806	0.0549	0.0623	1.0026	0.0632	0.0630
590	0.9707	0.0612	0.0630	1.1043	0.0708	0.0641
600	1.0641	0.0643	0.0604	1.2105	0.0750	0.0619
610	1.1671	0.0706	0.0605	1.3271	0.0815	0.0614
620	1.2755	0.0776	0.0608	1.4500	0.0892	0.0615
630	1.3971	0.0809	0.0579	1.5868	0.0949	0.0598
640	1.5963	0.0941	0.0589	1.8136	0.1073	0.0591
650	1.7363	0.1004	0.0578	1.9711	0.1184	0.0601
660	1.8912	0.1120	0.0592	2.1462	0.1315	0.0613
670	2.0517	0.1182	0.0576	2.3263	0.1388	0.0597
680	2.2284	0.1293	0.0580	2.5285	0.1564	0.0619

Table 2: High Voltage (V) vs. Resolution

The plot of Resolution vs. PMT High Voltage (V) is shown in Figure 41.

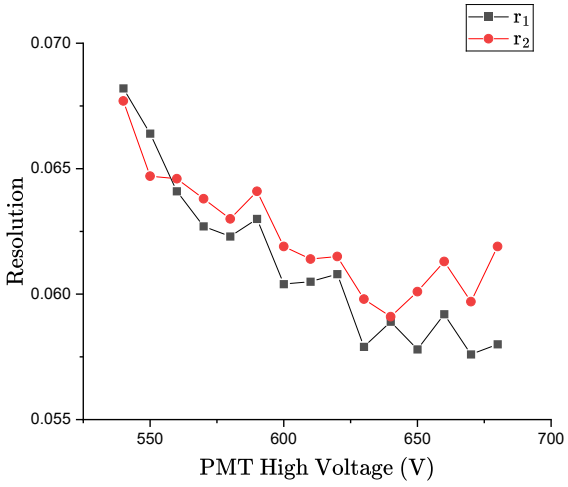

Figure 41: Resolution vs. PMT High Voltage (V)

Table 2 and Figure 41 show the variation of energy resolution with PMT high voltage for the two ^{60}Co photopeaks. The resolutions r_1 and r_2 correspond to the 1.17 MeV and 1.33 MeV peaks, respectively. As the applied voltage increases from 540 V to 680 V, the energy E_1 increases from 0.5582 MeV to 2.2284 MeV, and E_2 increases from 0.6377 MeV to 2.5285 MeV, indicating the expected gain amplification of the PMT with voltage.

The resolutions r_1 and r_2 show a clear decreasing trend with increasing voltage. At 540 V, $r_1 = 0.0682$ and $r_2 = 0.0677$, while at 680 V they reduce to $r_1 = 0.0580$ and $r_2 = 0.0619$. This implies that the detector's ability to distinguish between closely spaced energy peaks improves as the voltage increases, due to higher signal amplification and improved signal-to-noise ratio.

Quantitatively, between 540 V and 600 V, both resolutions drop significantly (from about 0.068 to 0.060), showing strong improvement in detector performance. Beyond 620 V, the rate of improvement becomes smaller, and the resolution values tend to stabilize around 0.058–0.061, suggesting that further increase in voltage yields diminishing returns.

Figure 41 confirms this behavior visually: both r_1 (black curve) and r_2 (red curve) follow a similar decreasing pattern with small fluctuations, showing close agreement throughout the voltage range. The slight oscillations beyond 650 V may arise from electronic noise or statistical uncertainty in peak fitting.

Overall, the graph and data indicate that optimal resolution occurs in the voltage range of approximately 640–670 V, where both r_1 and r_2 reach their minimum values (around 0.058–0.060). Thus, increasing PMT voltage improves resolution up to a point, after which further increase offers little improvement and may risk detector instability.

7 Sources of Error

7.1 Systematic Errors

1. **Energy Calibration Error:** Inaccurate determination of the channel centroids for calibration peaks of ^{60}Co can introduce systematic bias in calculated energies.

2. **PMT Voltage Drift:** Small drifts in the PMT high-voltage supply over time can cause gain instability and shift the peak positions.

3. **Electronic Nonlinearity:** Nonlinear response of amplifier or MCA ADC can slightly distort the proportionality between energy and channel number.

4. **Background Radiation:** Residual ambient background or scattering from laboratory walls can superimpose low-level counts on the spectrum.

5. **Geometric Uncertainty:** Variations in the source-detector distance and alignment affect the detected intensity and efficiency measurement.

7.2 Random Errors

1. **Statistical Fluctuations:** Due to the Poisson nature of radioactive decay, the number of detected counts in each channel fluctuates randomly, especially for shorter acquisition times.

2. **Photon Statistics in Scintillator:** Random variations in the number of scintillation photons and photoelectrons generated per event contribute to intrinsic resolution broadening.

3. **Electronic Noise:** Random noise from preamplifier and PMT dark current contributes to baseline fluctuations.
4. **Counting Statistics:** The relative uncertainty in measured counts follows $\frac{1}{\sqrt{N}}$, where N is total number of counts, limiting precision for weak sources.

8 Results

- The calibration of the MCA using ^{60}Co peaks yielded a linear relationship between energy and channel number:

$$E = aC + b, \quad \text{where } a \approx 3.4 \times 10^{-3}\,\text{MeV/channel},\ b \approx -3.8 \times 10^{-2}\,\text{MeV}.$$

- Using this calibration, the ^{137}Cs photopeak was found at ≈ 0.65 MeV, consistent with the known value of 0.662 MeV.
- The photopeak efficiencies of ^{60}Co were found to be approximately 0.09 for each of the 1.17 MeV and 1.33 MeV peaks, and for ^{137}Cs approximately 0.30, indicating higher detection efficiency at lower γ energy.
- The detector energy resolution ($\Delta E/E$) improved (i.e., decreased) with increasing PMT voltage up to a certain optimum range (around 640–670 V), beyond which electronic noise and pulse pile-up effects may dominate.
- The FWHM values and efficiency trends were consistent with theoretical expectations for NaI(Tl) scintillation detectors.

9 Conclusions

The γ-ray spectra of ^{60}Co and ^{137}Cs were successfully obtained and analyzed using a NaI(Tl) scintillation detector and a Multi-Channel Analyzer. Calibration using the dual γ peaks of ^{60}Co enabled accurate determination of the energy of the ^{137}Cs photopeak. The linear calibration constant was in good agreement with expected values.

The measured photopeak efficiencies demonstrate the strong dependence of detection efficiency on photon energy and detector geometry. The study of detector resolution as a function of PMT voltage showed that resolution improves with voltage up to an optimal level, confirming that PMT gain plays a crucial role in spectral sharpness.

Overall, the experiment validated the theoretical principles of γ-ray interaction with matter and the operation of scintillation detectors. The characteristic photopeaks, Compton continua, and background regions were clearly observed, providing insight into the processes of photoelectric absorption, Compton scattering, and partial energy deposition.

Directions for Future Use

- The setup can be extended to include additional calibration sources such as ^{22}Na or ^{137}Cs–^{60}Co mixed standards to test linearity over a wider energy range.
- Future experiments may employ high-purity germanium (HPGe) detectors for superior resolution and comparison with scintillator results.

- Background correction and dead-time analysis can be automated through MCA software scripting for improved precision.
- Measurements of efficiency as a function of source-detector distance can be performed to characterize geometric effects quantitatively.
- The experiment can be adapted to measure coincidence summing and cascade timing effects in γ-ray emission.

References

1. G. F. Knoll, *Radiation Detection and Measurement*, 4th ed., Wiley, 2010.
2. C. Grupen and B. Shwartz, *Particle Detectors*, 2nd ed., Cambridge University Press.
3. Alpen, E. L., *Radiation Biophysics*, 2nd ed., Academic Press, San Diego, CA, 1998.
4. Turner, J. E., *Atoms, Radiation, and Radiation Protection*, 2nd ed., Wiley-Interscience, New York, 1995.
5. Krane, K. S., *Introductory Nuclear Physics*, Wiley, 1987.
6. Firestone, R. B., and V. S. Shirley (eds.), *Table of Isotopes*, 8th edition, Wiley-Interscience, 1996.
7. NuDat 3.0, National Nuclear Data Center (NNDC), Brookhaven National Laboratory.
8. Leo, W. R., *Techniques for Nuclear and Particle Physics Experiments*, Springer, 1994.
9. Knoll, G. F., "Scintillation Detectors and Pulse-Height Spectroscopy," in *Radiation Detection and Measurement*, Ch. 5–6, Wiley, 2010.
10. Bevington, P. R., *Data Reduction and Error Analysis for the Physical Sciences*, 3rd ed., McGraw-Hill, 2003.
11. Gilmore, G. R., *Practical Gamma-Ray Spectrometry*, 2nd ed., Wiley, 2008.
12. Melissinos, A. C., *Experiments in Modern Physics*, Academic Press, 1966.

Appendix A: Full Experimental Data

The complete raw datasets corresponding to all γ-ray spectra recorded in this experiment are publicly available at the following online repository:

`https://github.com/KishalTandel/Lab-Reports/tree/main/Labs/Nuclear%20Physics/Report%203%20Data`